A MoTe$_2$-based light-emitting diode and photodetector for silicon photonic integrated circuits

Ya-Qing Bie[1]*, Gabriele Grosso[2], Mikkel Heuck[2], Marco M. Furchi[1], Yuan Cao[1], Jiabao Zheng[2,3], Darius Bunandar[1,2], Efren Navarro-Moratalla[1], Lin Zhou[2], Dmitri K. Efetov[2,4], Takashi Taniguchi[5], Kenji Watanabe[5], Jing Kong[2], Dirk Englund[2] and Pablo Jarillo-Herrero[1]*

One of the current challenges in photonics is developing high-speed, power-efficient, chip-integrated optical communications devices to address the interconnects bottleneck in high-speed computing systems[1]. Silicon photonics has emerged as a leading architecture, in part because of the promise that many components, such as waveguides, couplers, interferometers and modulators[2], could be directly integrated on silicon-based processors. However, light sources and photodetectors present ongoing challenges[3,4]. Common approaches for light sources include one or few off-chip or wafer-bonded lasers based on III–V materials, but recent system architecture studies show advantages for the use of many directly modulated light sources positioned at the transmitter location[5]. The most advanced photodetectors in the silicon photonic process are based on germanium, but this requires additional germanium growth, which increases the system cost[6]. The emerging two-dimensional transition-metal dichalcogenides (TMDs) offer a path for optical interconnect components that can be integrated with silicon photonics and complementary metal-oxide-semiconductors (CMOS) processing by back-end-of-the-line steps[7–9]. Here, we demonstrate a silicon waveguide-integrated light source and photodetector based on a p–n junction of bilayer MoTe$_2$, a TMD semiconductor with an infrared bandgap[10]. This state-of-the-art fabrication technology provides new opportunities for integrated optoelectronic systems.

The power consumption of interconnects is becoming increasingly problematic in high-performance computing systems. For instance, retrieving two floating point numbers can require an order of magnitude more energy than a logic operation between them[11,12]. Today, many high-performance computing applications require multiple domains to execute bandwidth-critical applications across many different parallel resources, often at intermittent but explosive data volumes. Recent theoretical studies[5] have shown that these rapidly shifting and intermittent communication requirements across computing domains favour multiple low-power direct-modulation light sources in place of one or few high-power lasers distributed across many transmitter modulators. The advantages of integrating light sources with electrical computing modules have increased the interest in layered two-dimensional (2D) materials, which have been demonstrated recently to possess promising properties for use in electronic and optoelectronic devices[13–16]. In contrast to covalently bonded materials produced by epitaxial growth, the van der Waals interaction between the 2D layers and the silicon substrate minimizes the introduction of surface defects

due to lattice mismatch[17–19]. MoTe$_2$ is a 2D semiconductor with a bandgap of ~1 eV at room temperature. The successful large-scale chemical vapour growth method used for MoTe$_2$ (refs 8,20) and h-BN (ref. 21) and 2D atomic thin material transfer methods[9,22] could enable practical optoelectronics applications in the near-infrared range[10,23,24]. In this Letter, we demonstrate MoTe$_2$-based lateral p–n junctions with an electrostatic split-gate configuration[14–16], which allows for diverse functionalities including transistors, light-emitting diodes (LEDs) and photodetectors, integrated with a silicon photonic-crystal (PhC) waveguide.

Figure 1a illustrates the MoTe$_2$ device. The p–n junction is designed to evanescently couple to the modes of the PhC waveguide, which is based on a holey silicon membrane. The device contains a grating coupler at the far end of the waveguide to allow excitation and collection. When the p–n junction is operated as an LED (top panel of Fig. 1a), the emitted light couples to the waveguide, where it travels in-plane to the grating coupler. In the photodetector mode, incident light is coupled into the waveguide by the grating coupler and detected by the p–n junction, which transforms it into an electrical signal. As illustrated in the device cross-section in Fig. 1b, the MoTe$_2$ p–n junction relies on an exfoliated bilayer of MoTe$_2$ separated by a hexagonal boron nitride (h-BN) dielectric layer from a split graphite gate to electrostatically induce the p- and n-type doping. The entire device is encapsulated by h-BN layers[7] to prevent natural oxidation of the MoTe$_2$.

Figure 1c shows the optical near-field coupling between the p–n junction and the waveguide, based on 3D finite-difference time-domain (FDTD) simulations. Emitted light from a dipole is used to represent the MoTe$_2$ emission, which is evanescently coupled into the waveguide, as expected. The final device is shown in the optical microscope image in Fig. 1d. Details of the simulation and device fabrication are described in the Methods, Supplementary Fig. 5 and Supplementary Note 4.

Figure 2a,b presents characteristic current–voltage (I_{ds}–V_{ds}) curves for different gate voltage configurations. All the electrical measurements were performed at room temperature in vacuum (10^{-4} torr) unless otherwise noted. The voltages on the two top graphite gates (V_{lg} for the left gate and V_{rg} for the right gate) independently control the carrier type and density on the two sides of the junction in the bilayer MoTe$_2$. As shown in Fig. 2a, the I_{ds}–V_{ds} curves are almost linear when both sides are p-doped (denoted PP, $V_{lg} = V_{rg} = -30$ V) or n-doped (denoted NN, $V_{lg} = V_{rg} = 30$ V). If the gates are oppositely biased, corresponding to a PN junction ($V_{lg} = -30$ V and $V_{rg} = 30$ V) or an NP junction ($V_{lg} = 30$ V and

[1]Department of Physics, Massachusetts Institute of Technology, Cambridge, Massachusetts 02139, USA. [2]Department of Electrical Engineering and Computer Science, Massachusetts Institute of Technology, Cambridge, Massachusetts 02139, USA. [3]Department of Electrical Engineering, Columbia University, New York, New York 10027, USA. [4]ICFO – Institut de Ciencies Fotoniques, The Barcelona Institute of Science and Technology, 08860 Castelldefels, Barcelona, Spain. [5]Advanced Materials Laboratory, National Institute for Materials Science, Tsukuba, Ibaraki 305-0044, Japan.
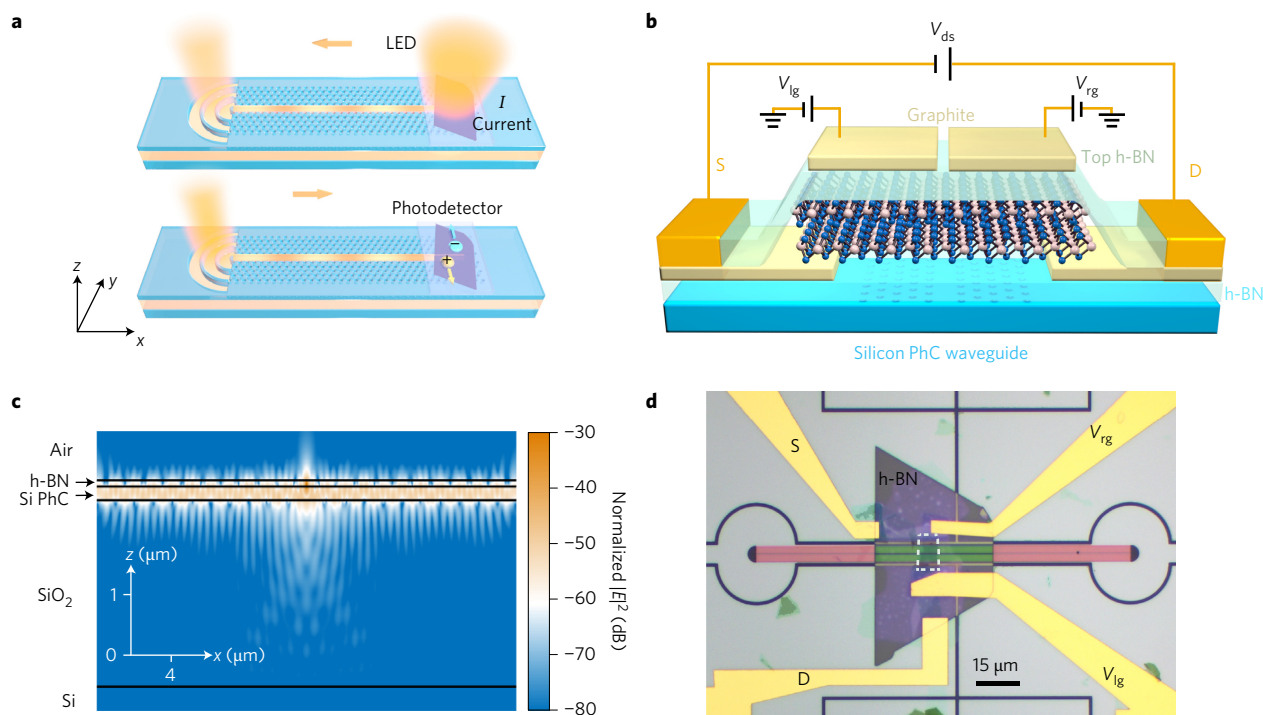*e-mail: yqbie@mit.edu; pjarillo@mit.edu

Figure 1 | Design of the waveguide-integrated LED and photodetector. a, In LED mode (top), the light emitted from the p–n junction propagates through the waveguide and is coupled out at the grating coupler. In photodetector mode (bottom), incident light is coupled to the waveguide through the grating coupler and is detected by the p–n junction. **b**, Cross-sectional schematic of the encapsulated bilayer MoTe$_2$ p–n junction on top of a silicon PhC waveguide. The carrier concentration in MoTe$_2$ is controlled by the split graphite gates, the separation of the two gates is 400 nm, the dielectric layer is h-BN on top of the MoTe$_2$, and the thickness is 80 nm. The source (S) and drain (D) electrodes are thin graphite flakes connected to Cr/Au leads. **c**, Cross-section of the electrical field intensity $|E|^2$ simulated by 3D FDTD. Coupling of light from the p–n junction into the waveguide is modelled using a y-polarized dipole source located 10 nm above the PhC waveguide encapsulated inside the h-BN. **d**, Microscopic image of the device. The white dashed line defines the bilayer MoTe$_2$ flake. The PhC waveguide is highlighted in pink and the two grating couplers at the edges are in black. Dark lines in the image are etched trenches designed to avoid short-circuiting.

$V_{rg} = -30$ V), we observe clear rectification behaviour (violet and green lines). To better analyse this rectification behaviour, Fig. 2b plots the PN and NP I_{ds}–V_{ds} curves on a semi-logarithmic scale, together with a fit by the Shockley model including a series channel resistance R_s (ref. 25). For the PN (NP) configuration, the diode threshold is 0.3 V (−0.3 V). In the forward bias region, a fit to the rapidly increasing current indicates a diode ideality factor of 2.3, which shows that carrier recombination dominates and the light emission originates from electron–hole recombination at the junction. The saturation behaviour of the current in the semi-logarithmic scale plot in the high forward bias regime gives $R_s = 0.6$ MΩ and $R_s = 0.25$ MΩ for the PN and NP configurations, respectively. R_s is the channel resistance in series with the PN (NP) junction, and the source–drain electrode separation is 10 μm. Current I_0 in the reverse bias region is ~10 pA, indicating a high-quality p–n junction interface.

Figure 2c,d plots the absolute value of I_{ds} as a function of V_{lg} and V_{rg} at fixed bias $V_{ds} = \pm 1$ V. The four corners of the figures correspond to the NN, PN, PP and NP configurations controlled by the split gate voltages. Figure 2e shows line-cuts of the current figures along the diagonal, where $V_g = V_{lg} = V_{rg}$. Because the left and right sides have the same doping level, the device is operating as a bipolar transistor with an on–off ratio of 1×10^5. Along the antidiagonal, the device can be tuned between the PN and NP configurations, as shown in Fig. 2f, which plots the gate-controlled rectification behaviour as a function of asymmetric gate voltage $V_j = (V_{lg} - V_{rg})/2$. These split gate-dependent I–V measurements show the versatility of the bilayer MoTe$_2$ device to function as an electrostatically controlled ambipolar transistor or p–n junction.

To explore the optical properties of bilayer MoTe$_2$, we measured photoluminescence (PL) and electroluminescence (EL) spectra at room and cryogenic temperatures, using a confocal microscope set-up with an infrared spectrometer and a camera (Supplementary Fig. 2). Figure 3a presents the EL spectra with $V_{lg} = -V_{rg} = -8$ V at a forward bias of $V_{ds} = 2$ V. The current is 2.3 μA at room temperature and 1.5 μA at low temperature. The figure also shows the PL at zero gate voltage for comparison. At room temperature, the EL and PL spectra are centred at 1,175 nm with a full-width at half-maximum (FWHM) of ~70 nm. At 6 K, the PL emission peak is narrowed to a FWHM of 10 nm centred at 1,090 nm. A small redshifted shoulder appears at 1,110 nm, which we attribute to the trionic peak. Trions are automatically created in the system due to intrinsic doping[26]. Both PL and EL peaks experience a blueshift with decreasing temperature (see Supplementary Figs 3a,b and 4a for details). To correlate the electrostatic doping level with the emission spectra, we configured the device as a bipolar transistor with a uniform gate voltage $V_g = V_{lg} = V_{rg}$. Figure 3b shows the PL intensity as a function of wavelength and gate voltage V_g at 6 K, where the excitonic (X^0) and trionic (X^+) peaks can be clearly distinguished. Further spectral analysis is provided in Supplementary Notes 2 and 3.

Figure 3c shows the EL intensity with the device in LED mode, overlaid on a false-colour optical image of the structure at room temperature. The strongest emission intensity originates from the p–n junction area where carrier recombination happens. A fraction of the emission that is coupled to the waveguide is scattered at the grating couplers, which lights up in the image under forward bias. We estimate the efficiency η of the photonic structure—that is, the fraction of EL photons collected from the grating couplers—as $\eta = (\gamma_{couplers}/(\gamma_{p-n} + \gamma_{couplers}))$, where $\gamma_{couplers}$ (γ_{p-n}) denotes the number of photons collected from the two grating couplers (the p–n junction), respectively. Based on the EL images, we estimate
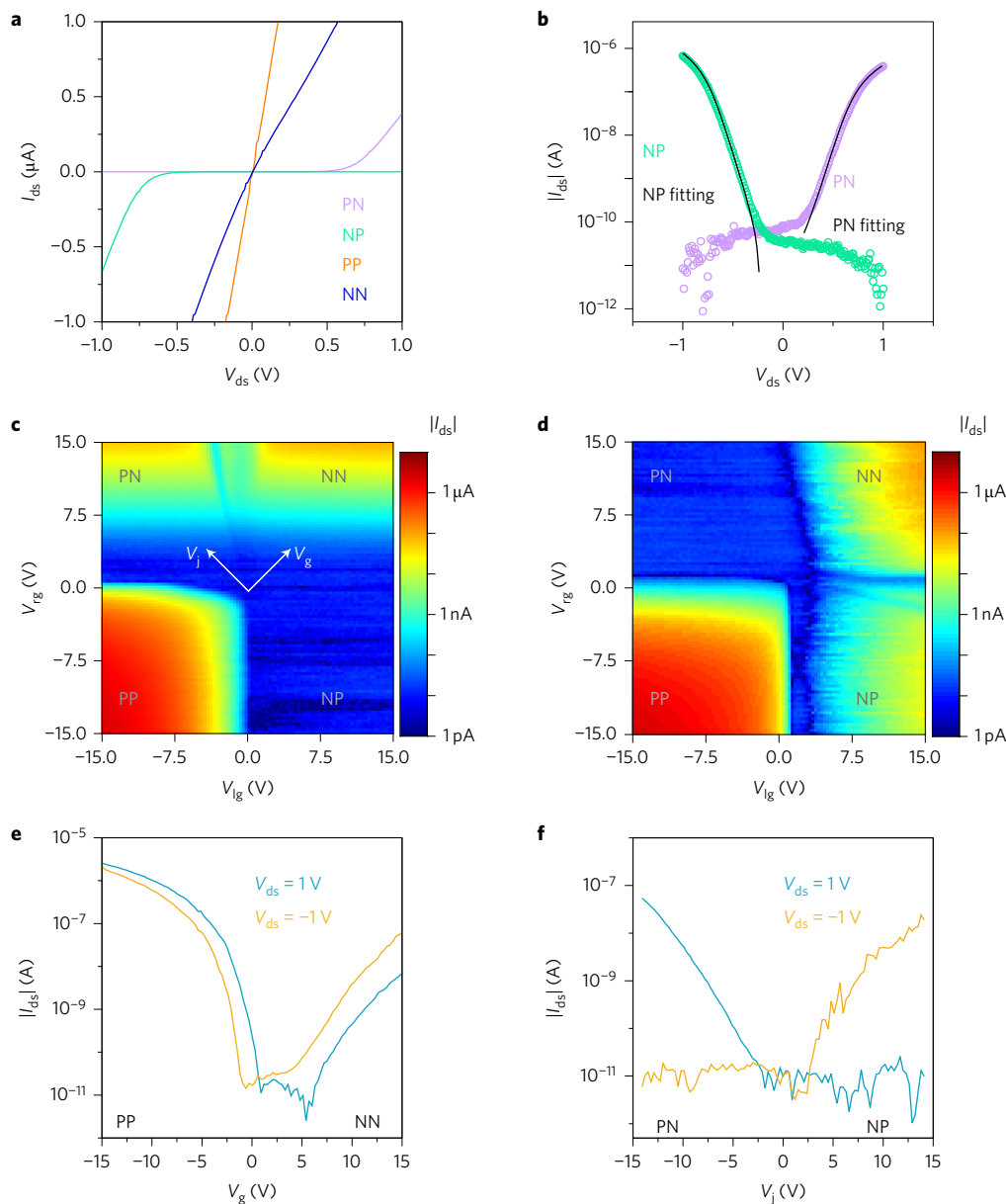
Figure 2 | Gate-controlled bilayer MoTe₂ p–n junction electrical properties at room temperature. a, I_{ds}–V_{ds} curves of the device at different doping levels plotted in linear scale. Gate voltages are set to ±30 V. **b**, $|I_{ds}|$–V_{ds} curves for PN (violet circles) and NP (green circles) junctions plotted on a semi-logarithmic scale. The diode ideality for both the PN and NP configurations is fitted to be n = 2.3. **c,d**, Current $|I_{ds}|$ flowing through the device as a function of split gate configuration shown on a logarithmic scale at a fixed bias voltage of V_{ds} = 1 V (**c**) or V_{ds} = –1 V (**d**). **e**, Diagonal line cuts of **c** (blue line) and **d** (yellow line), where both gates are swept together, $V_g = V_{lg} = V_{rg}$. These curves are characteristics of an ambipolar field-effect transistor. **f**, Off-diagonal line cuts of **c** and **d** show the dependence of current $|I_{ds}|$ as a function of asymmetric gate voltage $V_j = (V_{lg} - V_{rg})/2$.

that γ is ~5%, which includes the significant losses at the grating couplers and in the detection set-up. The emission at the left grating coupler is weaker because one piece of graphite was accidentally transferred onto the left side of the waveguide during the transfer process. The broadband absorption of graphene reduces the PhC mode on this arm of the device.

The selective detection offered by the confocal microscopy allows a comparison of the emission spectra from the different areas of the device. In Fig. 3d, the blue line plots the normalized EL emission spectrum collected from the grating coupler, showing a narrow peak (FWHM of ~10 nm) centred at 1,160 nm on top of a broader peak that matches the free-space emission of the bilayer MoTe₂ centred at 1,175 nm. For comparison, the transmission spectra of the silicon waveguide are also plotted before (orange line) and after (green line) MoTe₂ stack transfer. Here, the

transmission spectra were measured by sending broadband white light onto one grating coupler and collecting from the other coupler within the same field of view of the collection objective. The pre-transfer PhC transmission shows a peak at 1,160 nm, which matches well with the guided EL emission. After the MoTe₂ transfer, the peak transmission at 1,160 nm drops, as shown by the green line in Fig. 3d, mainly because of the MoTe₂ absorption that disturbs the PhC modes. However, as the p–n junction works as an LED, the MoTe₂ absorption is reduced because the excited states have been filled by electrically excited carriers and the waveguided light is not reabsorbed by the MoTe₂. Therefore, the peak at 1,160 nm due to the PhC mode recovers and is detected from the grating coupler in the EL emission spectrum (blue line). In addition to the narrow peak at 1,160 nm, the broader peak centred at 1,175 nm is the product of the LED
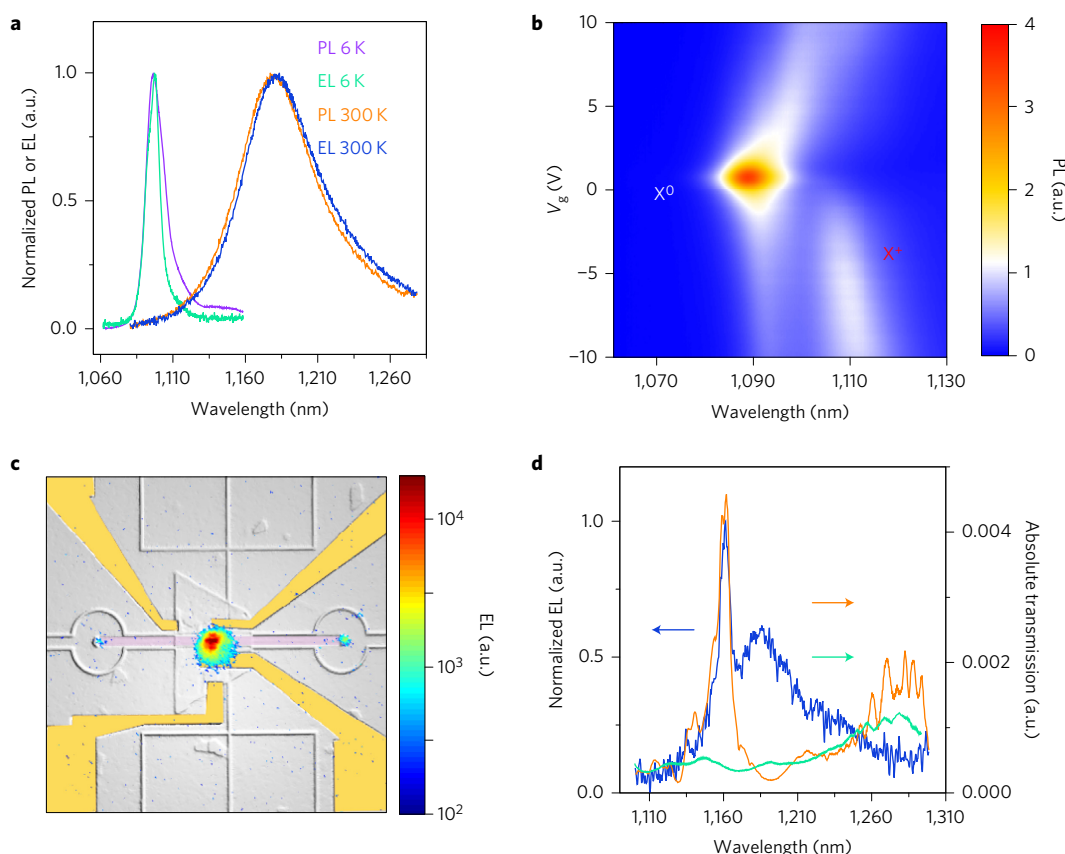
Figure 3 | Optical properties of the bilayer MoTe$_2$-silicon waveguide coupled device. a, Spectrally resolved PL of the bilayer MoTe$_2$ flake and EL of the MoTe$_2$ p–n junction at room temperature and at 6 K. The gate voltages of the p–n junction were set with opposite polarity $V_{lg} = -8$ V and $V_{rg} = 8$ V at a bias of $V_{ds} = 2$ V. **b**, Spectrally resolved PL map of the bilayer MoTe$_2$ at 6 K as a function of gate voltage $V_g = V_{lg} = V_{rg}$. The charge neutrality point is found to be at $V_{CNP} = 0.8$ V. The thickness of the dielectric h-BN layer is 35 nm for **a** and **b**. **c**, EL emission image at room temperature overlaid on top of a false-colour optical image of the device. Two extra emission spots from the grating couplers demonstrate coupling of the light source and silicon waveguide. **d**, Transmission of the waveguide before (orange) and after (green) transfer of MoTe$_2$. The blue line is the emission spectrum from the grating coupler. The thicknesses of the top and bottom h-BN layers are 80 and 10 nm, respectively, for other bilayer devices.

spectrum shown in Fig. 3a (300 K) and a flat broad transmission mode of the waveguide (green line). The shape of the broader emission is determined by the LED spectrum. Therefore, the guided EL spectrum reveals a mix of PhC waveguide mode (1,160 nm) and bilayer MoTe$_2$ emission (1,175 nm). Similar devices made of monolayer MoTe$_2$ have also been measured and the results are summarized in Supplementary Figs 6 and 7. Unlike other TMDs, emission from bilayer MoTe$_2$ at room temperature occurs through direct-bandgap optical transitions, similar to the monolayer[23,24,27]. Compared to the monolayer, bilayer MoTe$_2$ allows stronger optical and electrical excitation and has a longer emission wavelength below the silicon band-edge.

When the device is operated as a photodetector (Fig. 4a–c), the laser with wavelength at 1,160 nm is directed into the grating coupler, guided along the waveguide, and absorbed at the p–n junction, where a photocurrent is generated. Figure 4a plots the NP junction I–V curves for different incident laser powers. In reverse bias, the photocurrent generated by the incident laser at 19 µW is 2.5 nA, which is three orders of magnitude larger than the dark current. Figure 4b shows that the photocurrent at zero bias voltage increases linearly with laser power. The responsivity of the photodetector is calculated to be 4.8 mA W^{-1} by estimating that 2.5% of the incident laser power is guided to the p–n junction. Similarly, the external quantum efficiency (EQE) can be calculated as EQE = $(I_{sc}/P_{laser})/(hc/e\lambda)$ = 0.5% at a wavelength of 1,160 nm, where I_{sc}, P_{laser}, h, c and e are short-circuit current, laser power, Planck's constant, the speed of light and electron charge,

respectively. A detailed analysis of the responsivity is provided in Supplementary Note 7.

Unlike the reported photogating and photoconductive-type detectors based on few-layer MoTe$_2$ transistors[28–30], the bilayer MoTe$_2$ p–n junction shows a far higher response speed, as shown in Fig. 4c. Using the time-domain method, the photocurrent response bandwidth of the p–n junction is measured up to 200 MHz, limited only by the response speed of our current amplifier in the experimental set-up. From the consideration of built-in electrical field and drift velocity, we estimate that the p–n junction can achieve gigahertz bandwidth. More details are provided in Supplementary Note 6 and Supplementary Fig. 9.

Figure 4d plots the wavelength-dependent photocurrent, which shows that the photocurrent response originates from the guided, and not the scattered, light. The response peak is near 1,160 nm where the waveguide transmission is largest. Above 1,200 nm and below 1,110 nm, the photoresponse drops because of the reduced absorption of the bilayer MoTe$_2$ and the waveguide transmission cutoff. The MoTe$_2$ p–n junction can potentially be used to detect the emission from the MoTe$_2$ in an emitter–receiver configuration.

Our results demonstrate the integration of light-emitting diodes and photodetectors based on bilayer MoTe$_2$ p–n junctions with silicon PhC waveguide technologies. The integration of TMD LEDs into silicon photonics enables point-to-point optical links. Furthermore, narrowband lasers may be realized in a similar way, by integrating the electrically pumped TMD gain materials with PhC nanocavities, which can be coupled to waveguides with near-
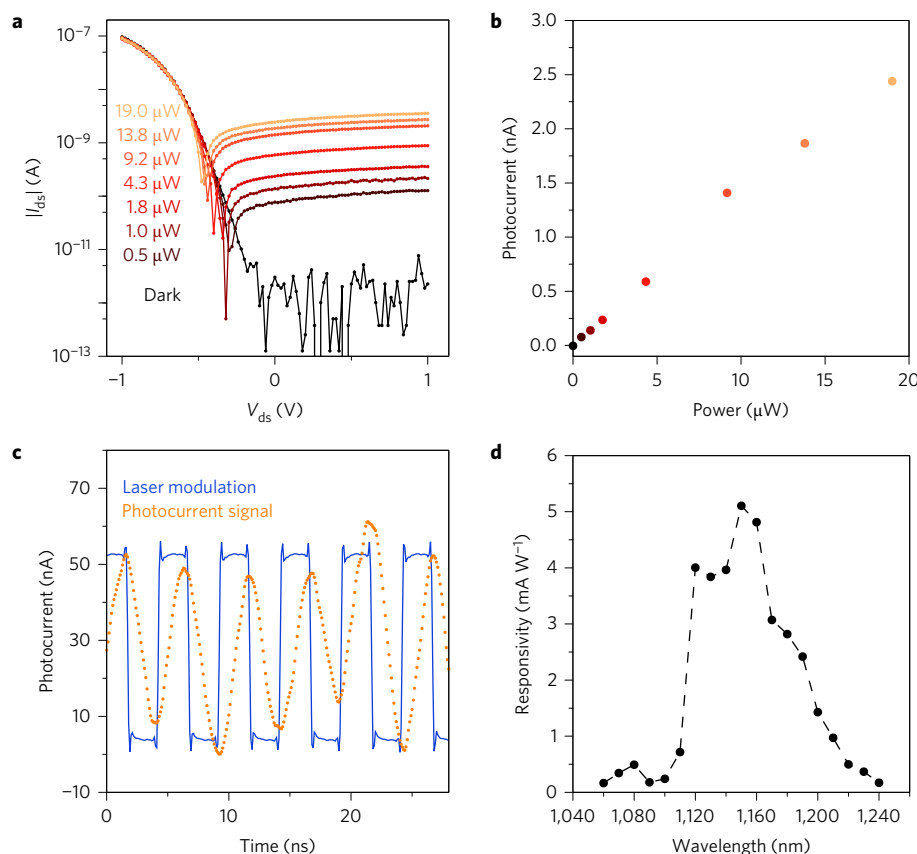
Figure 4 | Photocurrent response of a bilayer MoTe$_2$ NP junction integrated into the silicon waveguide at room temperature. a, I_{ds}–V_{ds} curves are plotted on a semi-logarithmic scale for incident laser power on the grating coupler between zero and 19 μW at V_{lg} = 15 V and V_{rg} = –15 V. **b**, Short-circuit (V_{ds} = 0 V) photocurrent I_{sc} at different laser powers. **c**, The photocurrent is turned on and off at zero bias with modulated laser excitation shining at the p–n junction (high and low signal, respectively). **d**, Wavelength-dependent responsivity of the waveguide-integrated photodetector.

unity efficiency[31], which could further increase the optical coupling efficiency and allow for on-chip waveguide division multiplexing. Given the rapid advancements of devices based on 2D van der Waals materials, novel functionalities and better performance can be expected[32]. For example, the interlayer exciton emission and electrostatic gating effect provides extra tuning capabilities for the emission wavelength, while the use of heterostructures that allow exciton emission in the near-infrared (NIR) range could provide more efficient active layers for light emission, and higher-speed data communications can be expected by integrating with large-bandwidth graphene modulators[13]. Moreover, this work shows that all active optical components for point-to-point interconnects are possible with 2D TMD devices transferred onto otherwise passive photonic integrated circuits. We emphasize that a silicon waveguiding layer is not the only choice; our approach is compatible with passive waveguide layers, such as silicon nitride, which are available as top layers in most CMOS processes. This ease of integration on a wide range of electrical processors and memory has the potential to greatly simplify the design of high-speed interconnects in advanced computing and sensor systems.

Methods

Methods and any associated references are available in the online version of the paper.

References

1. Miller, D. A. B. Device requirements for optical interconnects to silicon chips. *Proc. IEEE* **97**, 1166–1185 (2009).
2. Reed, G. T. in *Silicon Photonics: The State of the Art* 15–145 (Wiley, 2008).
3. Pyatkov, F. *et al.* Cavity-enhanced light emission from electrically driven carbon nanotubes. *Nat. Photon.* **10**, 420–427 (2016).
4. Birowosuto, M. D. *et al.* Movable high-Q nanoresonators realized by semiconductor nanowires on a Si photonic crystal platform. *Nat. Mater.* **13**, 279–285 (2014).
5. Bergman, K., Carloni, L. P., Biberman, A., Chan, J. & Hendry, G. *Photonic Network-on-Chip Design* (Springer, 2014).
6. Famà, S., Colace, L., Masini, G., Assanto, G. & Luan, H.-C. High performance germanium-on-silicon detectors for optical communications. *Appl. Phys. Lett.* **81**, 586–588 (2002).
7. Wang, L. *et al.* One-dimensional electrical contact to a two-dimensional material. *Science* **342**, 614–617 (2013).
8. Zhou, L. *et al.* Large-area synthesis of high-quality uniform few-layer MoTe$_2$. *J. Am. Chem. Soc.* **137**, 11892–11895 (2015).
9. Kang, K. *et al.* High-mobility three-atom-thick semiconducting films with wafer-scale homogeneity. *Nature* **520**, 656–660 (2015).
10. Ruppert, C., Aslan, O. B. & Heinz, T. F. Optical properties and band gap of single- and few-layer MoTe$_2$ crystals. *Nano Lett.* **14**, 6231–6236 (2014).
11. Shacham, A., Bergman, K. & Carloni, L. P. Photonic networks-on-chip for future generations of chip multiprocessors. *IEEE Trans. Comput.* **57**, 1246–1260 (2008).
12. Borkar, S. & Chien, A. A. The future of microprocessors. *Commun. ACM* **54**, 67–77 (2011).
13. Liu, M. *et al.* A graphene-based broadband optical modulator. *Nature* **474**, 64–67 (2011).
14. Pospischil, A., Furchi, M. M. & Mueller, T. Solar-energy conversion and light emission in an atomic monolayer p–n diode. *Nat. Nanotech.* **9**, 257–261 (2014).
15. Baugher, B. W. H., Churchill, H. O. H., Yang, Y. & Jarillo-Herrero, P. Optoelectronic devices based on electrically tunable p–n diodes in a monolayer dichalcogenide. *Nat. Nanotech.* **9**, 262–267 (2014).
16. Ross, J. S. *et al.* Electrically tunable excitonic light-emitting diodes based on monolayer WSe$_2$ p–n junctions. *Nat. Nanotech.* **9**, 268–272 (2014).
17. Palacios, T. Graphene electronics: thinking outside the silicon box. *Nat. Nanotech.* **6**, 464–465 (2011).
18. Fiori, G. *et al.* Electronics based on two-dimensional materials. *Nat. Nanotech.* **9**, 768–779 (2014).
19. Ferrari, A. C. *et al.* Science and technology roadmap for graphene, related two-dimensional crystals, and hybrid systems. *Nanoscale* **7**, 4598–4810 (2015).

20. Naylor, C. H. *et al.* Monolayer single-crystal 1T′-MoTe$_2$ grown by chemical vapor deposition exhibits weak antilocalization effect. *Nano Lett.* **16,** 4297–4304 (2016).
21. Kim, S. M. *et al.* Synthesis of large-area multilayer hexagonal boron nitride for high material performance. *Nature Commun.* **6,** 8662 (2015).
22. Ma, D. *et al.* A universal etching-free transfer of MoS$_2$ films for applications in photodetectors. *Nano Res.* **8,** 3662–3672 (2015).
23. Lezama, I. G. *et al.* Indirect-to-direct band gap crossover in few-layer MoTe$_2$. *Nano Lett.* **15,** 2336–2342 (2015).
24. Robert, C. *et al.* Excitonic properties of semiconducting monolayer and bilayer MoTe$_2$. *Phys. Rev. B* **94,** 155425 (2016).
25. Banwell, T. & Jayakumar, A. Exact analytical solution for current flow through diode with series resistance. *Electron. Lett.* **36,** 291–292 (2000).
26. Ross, J. S. *et al.* Electrical control of neutral and charged excitons in a monolayer semiconductor. *Nat. Commun.* **4,** 1474 (2013).
27. Froehlicher, G., Lorchat, E. & Berciaud, S. Direct versus indirect band gap emission and exciton–exciton annihilation in atomically thin molybdenum ditelluride MoTe$_2$. *Phys. Rev. B* **94,** 085429 (2016).
28. Hai, H. *et al.* Highly sensitive visible to infrared MoTe$_2$ photodetectors enhanced by the photogating effect. *Nanotechnology* **27,** 445201 (2016).
29. Yin, L. *et al.* Ultrahigh sensitive MoTe$_2$ phototransistors driven by carrier tunneling. *Appl. Phys. Lett.* **108,** 043503 (2016).
30. Octon, T. J., Nagareddy, V. K., Russo, S., Craciun, M. F. & Wright, C. D. Fast high-responsivity few-layer MoTe$_2$ photodetectors. *Adv. Opt. Mater.* **4,** 1750–1754 (2016).
31. Akahane, Y., Asano, T., Song, B.-S. & Noda, S. Fine-tuned high-Q photonic-crystal nanocavity. *Opt. Express* **13,** 1202–1214 (2005).
32. Shiue, R.-J. *et al.* High-responsivity graphene–boron nitride photodetector and autocorrelator in a silicon photonic integrated circuit. *Nano Lett.* **15,** 7288–7293 (2015).

Author contributions
Y.Q.B., D.E. and P.J.-H. conceived the experiment. Y.Q.B., J.Z., E.N.-M. and L.Z. fabricated the samples. Y.Q.B., G.G., M.M.F., Y.C. and D.B. performed the measurements. M.H. simulated the photonic crystal waveguide. L.Z. and D.K.E. participated in early discussions and experiments. T.T. and K.W. grew the crystals of hexagonal boron nitride. J.K., D.E. and P.J.-H. advised on the experiments and data analysis. All authors discussed the results and commented on the manuscript.

Additional information
Supplementary information is available in the online version of the paper. Reprints and permissions information is available online at www.nature.com/reprints. Publisher's note: Springer Nature remains neutral with regard to jurisdictional claims in published maps and institutional affiliations. Correspondence and requests for materials should be addressed to Y.-Q.B. and P.J.-H.

Competing financial interests
The authors declare no competing financial interests.

Methods

Fabrication of encapsulated MoTe$_2$ p–n junctions. Device fabrication began with exfoliation on SiO$_2$/Si substrates of bulk MoTe$_2$ (from 2D semiconductors, HQ graphene or grown in-house using a chemical vapour transport technique), h-BN and natural graphite crystals. The graphite layer was then prepatterned to match the split-gate geometry. Monolayer and bilayer MoTe$_2$ were identified by optical contrast and PL. The target thin flakes were picked up by the transfer slide, composed of a stack of glass, a polydimethylsiloxane (PDMS) film and a polycarbonate (PC) film, as described in ref. 33. We picked up the flakes for stacking in the following order: graphite gate layer, top h-BN layer, bilayer MoTe$_2$, two pieces of thin graphite for electrodes and the bottom h-BN layer. The resulting stack was then placed on top of the PhC waveguide with the help of a transfer set-up that allowed a precision of 500 nm under an optical microscope. The alignment of the split graphite gate with the waveguide channel was subsequently verified by atomic force microscopy (AFM; for AFM images see Supplementary Fig. 1). The split gates were separated by a 400 nm gap, patterned using electron-beam lithography and reactive ion etching with oxygen plasma. The graphite thicknesses for both split gates and source drain electrodes were ~3–5 nm. The top h-BN worked as a dielectric layer with a dielectric constant ε_r of 3.9. In the device measured in Fig. 3a,b and Supplementary Figs 3 and 4, 35-nm-thick h-BN was used as the dielectric layer, but for the other bilayer devices, the thickness of the dielectric h-BN layer was 80 nm. The thickness of the bottom h-BN, which separates the MoTe$_2$ layer and the waveguide, was 10 nm.

Waveguide design. The PhC waveguide was designed to support a transverse-electric-like (TE-like) mode at wavelengths within the MoTe$_2$ emission range. Simulations were carried out using commercially available FDTD software (Lumerical). This software includes a frequency-dependent complex refractive index for the silicon layers. In the simulations, we included the bottom silicon substrate, the SiO$_2$ layer (3 μm), the silicon PhC membrane (220 nm) and a top h-BN layer of 100 nm thickness. The coupling of light emitted from the p–n junction into the waveguide was modelled using a dipole source (directed perpendicular to the x–z plane) located 10 nm above the silicon PhC membrane at the centre of the waveguide.

Fabrication of the PhC waveguide. Fabrication of the PhC device was carried out on an silicon on insulator chip with a 220 nm silicon device layer. Because the top silicon film is conductive, several trenches were etched to separate the electrodes and avoid short circuits. The PhC waveguide was 140 μm long and was designed with lattice constant a ranging from 271 to 298 nm and an air hole radius of $r = 0.25a$. The PhC patterns were defined by electron-beam lithography (JEOL JBX-6300FS, 100 keV) on a 150-nm-thick ZEP520A resist layer. Cold development with hexyl acetate was used to improve the pattern contrast. Patterns were then transferred from the electron-beam resist layer to the Si device layer using plasma etching with an SF$_6$ and O$_2$ gas mixture (SF$_6$:O$_2$ = 40:18) at cryogenic temperature (Oxford Instruments Plasmalab 100). A scanning electron micrograph (SEM) of the resultant device is shown in Supplementary Fig. 5a, and the lattice-constant-dependent waveguide transmission spectra are shown in Supplementary Fig. 5b.

Data availability. The data that support the findings of this study are available from the corresponding authors upon reasonable request.

References

33. Zomer, P. J., Guimarães, M. H. D., Brant, J. C., Tombros, N. & van Wees, B. J. Fast pick up technique for high quality heterostructures of bilayer graphene and hexagonal boron nitride. *Appl. Phys. Lett.* **105,** 013101 (2014).